Dimensional transformation and morphological control of graphitic carbon nitride from water-based supramolecular assembly for photocatalytic hydrogen evolution: from 3D to 2D and 1D nanostructures

Bing-Xin Zhou[a], Shuang-Shuang Ding[a], Bei-Jing Zhang[a], Lei Xu[a], Ruo-Shi Chen[a], Leng Luo[a], Wei-Qing Huang[a,*], Zhong Xie[a], Anlian Pan[b], Gui-Fang Huang[a,*]

[a] Department of Applied Physics, School of Physics and Electronics, Hunan University, Changsha, 410082, China
[b] School of Materials Science and Engineering, Hunan University, Changsha, 410082, China

ARTICLE INFO

ABSTRACT

Geometric dimensionality and morphology largely affect the properties and functionalities of materials; however, simultaneously regulating them to realize synergic effects is a formidable scientific and technological challenge. Here we demonstrate an effective strategy to control the dimensionality and morphology of graphitic carbon nitride (g-C_3N_4) through heat treatment the melamine-cyanuric acid supramolecular precursors formed in water as a "green" solvent. By varying heat treatments, the three-dimensional (3D) hexagonal prism precursors could be transformed to 3D g-C_3N_4 loofah-like (CNl) architectures, ultrathin two-dimensional (2D) g-C_3N_4 nanosheets (CNs), and ordered one-dimensional (1D) g-C_3N_4 nanotube (CNt) array, respectively. The adsorbed melamine molecules on the surface of precursor and atmosphere in the transformation process, play a key role in determining the morphology of products. The resulting ultrathin 2D CNs have a porous structure, a small thickness (1.6 nm), a large surface area (208.8 $m^2 \cdot g^{-1}$), and high conductivity, thus exhibiting higher hydrogen evolution rate (23.9 μmol h^{-1}) by 17.3 times than the bulk g-C_3N_4 (CN) under visible light irradiation. This strategy results in high-quality, ultrathin CNs at yields of ~10 wt% from raw material, much higher than those of previous reports (~6 wt% from bulk CN). This work not only enriches our understanding of the relationship between geometric dimensionality, morphology and properties of photocatalytic nanomaterials, but also could be potentially useful for the design and growth of 1D or 2D flexible polymers for energy-related applications and beyond.

1. Introduction

Geometric dimensionality and morphology play crucial roles in defining the properties and functionalities of materials. As a three-dimensional (3D) bulk material transforms into two-dimensional (2D) or one-dimensional (1D) structure, its electronic structure and optical properties alter due to quantum confinement and surface effects [1–3]. The change of geometric properties, such as increased specific surface area, caused by dimensional transformation, is of prime importance in many fields ranging from energy storage and conversion [4], catalysis [5–7], photocatalysis [8], adsorption, and sensing to biomedicine [9,10]. Despite much research, the preparation of 2D or 1D nanomaterials with desirable morphology for tuning their shape-dependent physical properties [11], which are consequently useful in applications (for instance, in photocatalysis) [12], is still a great challenge, which

can be understood by the lack of a general and conventional strategy that could be used as an effective guideline to control both dimensionality and morphology. Hence, much effort has been made to adjust the geometric properties of nanomaterials. A common approach widely used is hard (or soft) template method, which the morphology of products mainly depends on that of template [13,14]. However, it becomes powerless once it is associated with the preparation of ultrathin 2D nanosheets with a thickness of less than 2 nm [15–17].

In contrast to covalent compounds, for which the covalent bonds are strong, the dimensionality and morphology of flexible layered polymers are easier to adjust. Recently, g-C_3N_4, as a typical flexible layered polymer, has attracted increasing attention because of its advantages of easy fabrication, low cost [18], excellent stability against oxidation and corrosive chemical environments [19], and great potential for energy storage [20], water splitting [21–23], organic syntheses [24], and CO_2

capture and reduction [25,26]. In the specific case of photocatalysis, bulk 3D architectures have two main disadvantages: low specific surface area and high electron-hole recombination probability. These shortcomings of bulk g-C_3N_4 can largely be addressed by dimensional transformation (3D to 2D or 1D) and morphological tuning [27]. Various g-C_3N_4 nanostructures, including hollow spheres [28,29], nanoseaweeds [30], nanorods [31–33], nanosheets [34–36] and nanotubes [37–39] have been prepared and display enhanced photocatalytic performance with respect to their bulk counterparts. Among them, ultrathin 2D nanosheets is of great benefit for mass transport [40], light harvesting, and the contact of the catalyst surface with the reactants, due to the highly opened-up flat structure and enlarged surface area, which remarkably shortens the perpendicular migration distance of photogenerated charge from the bulk to the surface [41], and improve photogenerated charge transport along the in-plane direction, thus cooperatively working to minimize energy loss via radioactive charge recombination.

To prepare the 2D g-C_3N_4 nanosheets, various methods have been developed, including ultrasonication-assisted liquid exfoliation [42], concentrated acid [43,44] and thermal exfoliating [45,46]. For instance, bulk g-C_3N_4 could be exfoliated by concentrated H_2SO_4 [47] to nanosheets with a high BET surface area 206 $m^2 g^{-1}$(Table S3). However, these methods are not time- or cost-efficient and the thermal oxidation etching affords only ~6 wt% yield from bulk g-C_3N_4 [48]. By contrast, the supramolecular preorganization, which provides an easy control over structure by assembling monomers (like melamine, cyanuric acid, barbituric acid or derivatives) into supramolecular aggregates via hydrogen bonding, is a self-templating method to tune dimensionality and morphology of materials [49–52]. An attracting supramolecular precursor is composed of melamine and cyanuric acid in a solvent such as dimethyl sulfoxide (DMSO) [53] and ethanol [54]. These supramolecular precursor can be used to prepare various g-C_3N_4 structures including mesoporous, hollow spheres [55], microspheres [56], and hollow boxes [57]. However, the morphology of g-C_3N_4 obtained primarily depends on that of the precursor, and little ultrathin g-C_3N_4 nanosheets with large BET surface area have been reported from supramolecular precursors (Table S3).

Herein, we first report that 3D CN*l* architectures, 2D ultrathin CN*s*, and ordered 1D CN*t* array of g-C_3N_4 nanostructures can be constructed through a thermal treatment of 3D hexagonal prism supramolecular precursors obtained in water as a "green" solvent. The evolution of geometric dimensionality and morphology largely depends on the post treatment parameters and atmospheres. The resulting 2D ultrathin CN*s* have a porous structure, a small thickness (about 1.6 nm), and a large surface area (208.8 $m^2 g^{-1}$), thus exhibiting higher hydrogen evolution rate (HER, 23.9 μmol h^{-1}) by 17.3 times than the bulk CN under visible light irradiation. This strategy results in ultrathin CN*s* at yields of ~10 wt% from raw material, much higher than those of previous reports (~6 wt% from bulk CN).The present results not only enrich our understanding of the relationship between geometric dimensionality, morphology and properties of photocatalytic nanomaterials but also could be potentially useful for the design and growth of 1D or 2D flexible polymers.

2. Experimental section

2.1. Fabrication of g-C_3N_4

2.1.1. Bulk CN

Typically, 1 g melamine was placed in a crucible which was wrapped with tin foil. Afterward the crucible was heated at 500 °C for 2 h under the air atmosphere, with a heating rate of 5 °C min^{-1}.

2.1.2. CNl, CNt and CNs

Firstly, 1 g melamine and 1 g cyanuric acid were respectively dissolved into 50 mL hot water (90 °C) under continuous stirring. The

molar ratio of melamine to cyanuric acid is 1.02:1. After completely dissolved, the melamine solution was slowly dropped into cyanuric acid solution and white precipitate was quickly produced. After complete evaporation of the water, white melamine-cyanuric acid (M-CA) complexes left in the beaker were collected and dried at 60 °C overnight. Then the M-CA complexes were placed in a crucible wrapped with tin foil. Afterward the crucible was heated at 500 °C for 2 h in muffle furnace under the air atmosphere, with a heating rate of 5 °C min^{-1}. The obtained sample was labeled CN*l*. The CN*t* was obtained by heated (same conditions as CN*l*) M-CA complexes that were washed three times with ethanol and completely dried. The CN*s* was obtained by heated (500 °C for 3 h in tube furnace under the protection of N_2, with a heating rate of 5 °C min^{-1}) M-CA complexes that were washed three times with ethanol and completely dried.

2.2. Characterizations

The morphological details of all the samples were probed by an S-4800 field emission scanning electron microscopy (SEM) operating at an accelerating voltage of 5 kV. Transmission electron microscopy (TEM) studies were carried out using FEI Tecai-F20 scanning TEM. Powder X-ray diffraction (XRD) patterns of the samples were recorded on a Bruker D8 advance using CuKα radiation (40 kV, 40 mA, λ =0.1543 nm). X-ray photoelectron spectroscopy (XPS) measurement was conducted using an ESCALAB Mk2 system (Vacuum Generators) with Mg-Kα. Brunauer–Emmett–Teller (BET) surface area analysis was analyzed using the nitrogen adsorption method with a surface analyzer system (tri-star 3020). The photoluminescence (PL) spectras were measured by an F-2500 fluorescence spectrometer with pulsed xenon discharge lamps at room temperature. UV–vis diffuse reflectance spectra (DRS) was obtained from a Shimadzu UV3600 spectrophotometer equipped with a 60 mm diameter integrating sphere using $BaSO_4$ as reference. Thermal gravimetric analysis (TGA) and differential scanning calorimetry (DSC) experiments were carried out using the NETZSCH STA449C thermal analyzer to study the thermal decomposition behavior. The temperature range of the analyses were from room temperature to 600 °C, and the heating rate was 10 °C min^{-1} in air atmosphere.

2.3. Photoelectrochemical measurements

The electrochemical and photoelectric properties were performed on a CHI660B electrochemical system (Shanghai, China) using a standard three-electrode cell with a working electrode, a platinum wire counter electrode, and an Ag/AgCl reference electrode. Na_2SO_4 (0.1 M) was used as the electrolyte solution. All the electrochemical measurements were performed under room temperature (25 °C). To prepare the working electrode, 1 mg carbon nitride catalyst with 0.5 ml ethanol and 25 ul Nafion solution (5% vol%) were mixed ultrasonically for 30 min. Then, the suspension was dip-coating onto the F-doped tin oxide (FTO) glass electrode (1 × 1 cm^2) with heating at 80 °C. The electrochemical impedance spectroscopy (EIS) measurements were performed in a three-electrode cell in the presence of 5 mM $[Fe(CN)_6]^{3-}/[Fe(CN)_6]^{4-}$ by applying an AC voltage with 5 mV amplitude in a frequency range from 0.01 Hz to 100 kHz under open circuit potential conditions. The EIS datas were analyzed with Zview software. Mott-Schottky (M–S) analysis was performed in $NaSO_4$ by applying a potential range of −0.4–0.5 V vs. Ag/AgCl with a frequency of 10 kHz and an amplitude of 10 mV.

2.4. Photocatalytic hydrogen evolution

Photocatalytic hydrogen evolution was carried out in a gas tight system with a 450 mL side-irradiation Pyrex cell. Typically, 50 mg of catalysts were dispersed in an aqueous solution (333 mL) containing methanol (10 vol%) as sacrificial reagent. Co-catalyst (1 wt% Pt) was
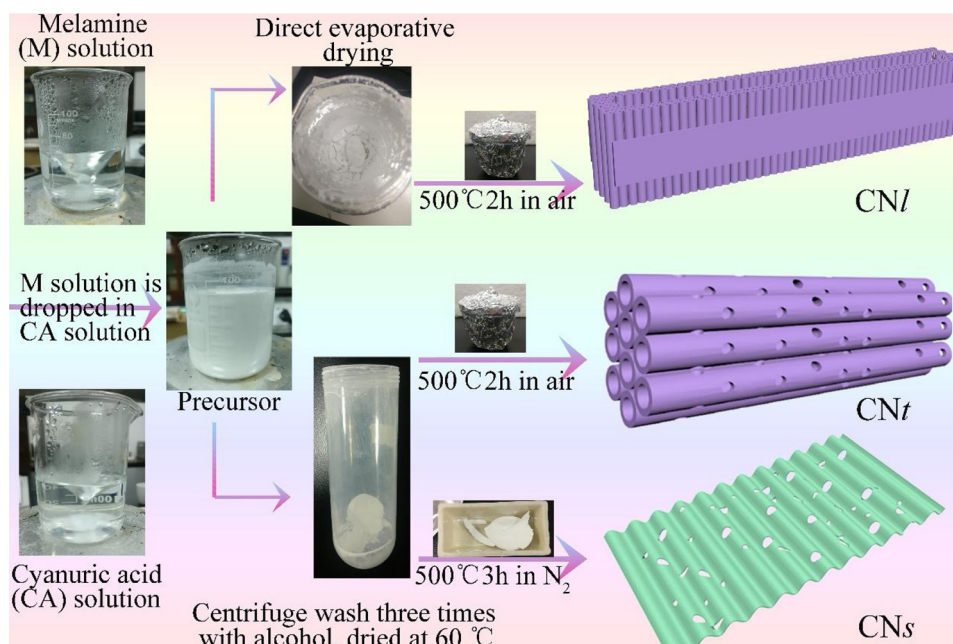
Fig. 1. Fabrication process of CN*l*, CN*t* and CN*s*.

introduced by in-situ photodeposition from the precursor of $H_2PtCl_6 \cdot 6H_2O$. The reaction solution was evacuated several times to completely remove air prior to irradiation. The reaction was conducted under a 300 W Xeon-lamp equipped with a 420 nm-cut-off filter. The evolved gas was analyzed by gas chromatography equipped with a thermal conductive detector (TCD) and a 5 Å molecular sieve column, using argon gas as the carrier gas.

3. Results and discussion

Supramolecular M−CA complexes are firstly prepared by mixing melamine and cyanuric acid in hot water (90 °C) (Fig. 1). SEM images show that the hexagonal prism M−CA complexes with smooth surface are formed as melamine and cyanuric acid are used in equal mass (here, 1 g), as shown in Fig. 2a. The slight non-equimolecular ratio of melamine and cyanuric acid (1.02 : 1) results in the residual melamine molecules adsorbed on M−CA complexes as shown in Fig. S1. The formation of the M−CA complex is evidenced by Fourier transform infrared (FT-IR) spectrum (Fig. S2). The shift of the triazine ring vibration of melamine to a lower wavenumber (from 814 cm^{-1} to 769 cm^{-1}) indicate the presence of hydrogen bonding between melamine and cyanuric acid. The results are consistent with the previous reports. [57] Evidence for the existence of free melamine molecules on the surface of the M−CA complexes can be confirmed via the stretching vibration of melamine at about 814 cm^{-1} with an asymmetric peak. In addition, the adsorbed melamine molecules on the M−CA complexes can be removed through ethanol washing as illustrated in Fig. S2. The free melamine molecules on the surface of the M−CA complexes can be preferentially decomposed and release gases such as CO_2 and NH_3 as confirmed by TGA test (Fig. S3) [53]. To produce g-C_3N_4 crystals, three different post treatments were conducted on M−CA complexes, which results into the obtained g-C_3N_4 with different geometric dimensionality and morphology (Fig. 2). The 3D CN*l* is produced when the M−CA complexes are directly evaporated to dryness and subsequent heated in the crucible covered and wrapped with tinfoil at 500 °C for 2 h under an air atmosphere, as shown in Fig. 1. In contrast, 2D CN*s* and 1D CN*t* can be prepared from the hexagonal prism M−CA complexes as they are washed three times with ethanol and subsequent treatments in N_2 and air atmospheres, respectively.

The SEM (Fig. 2 b1) and TEM (Fig. 2 b2, b3) images display that the

3D CN*l* with a porous hierarchical self-supporting hollow structure is composed of nanosheets and nanotubes. Fig. 2 c1-c3 show that the ordered CN*t* array is a 1D hollow structure with abundant mesopores on the tube wall, which are of great significance for the chemical processes. Under inert atmosphere (N_2), unexpectedly, the M-CA complexes evolve into 2D porous ultrathin nanosheets with chiff;on-like ripples and wrinkles resulting from the deformation and distortion, as clearly shown in Fig. 2d and Fig. S5. The dark contrast lines in these images (Fig. 2d2) are believed to be the standing edges or wrinkles of CN*s*. To gain the insight into the morphology and thickness of these nanosheets, atomic force microscopy (AFM) images were recorded. Fig. 2d4 shows that the resulting CN*s* that are cast on a silicon wafer are flat, with a thickness of ~1.6 nm (about 5 layers). Most studies available to date report that the morphology of g-C_3N_4 obtained from supramolecular precursors is either irregular shape, or depends on that of the precursors [58]. This is, therefore, the first to tune both the geometric dimensionality and morphology of g-C_3N_4 through different post treatments of the same precursor.

To elucidate the mechanism of dimensional and morphological transformation, the microstructure evolution of the M-CA complex during the annealing process is shown in Fig. 3. The shape of hexagonal prism M-CA complexes could be basically maintained in air as the annealing temperature is below 500 °C, and that are subsequently thermally etched into CN*l* with porous hierarchical structure due to the release of various gases including CO_2 and NH_3 (the upper panel of Fig. 3). This may be due to the presence of melamine molecules adsorbed on the 3D hexagonal prism M-CA complexes formed from 1.02 : 1 M ratio of melamine and cyanuric acid in water and dried via directly evaporation. The residual free melamine molecules adsorbed on M-CA complexes preferentially decompose and consume oxygen in the crucible covered and wrapped with tinfoil. Simultaneously, the derived gases such as CO_2 and NH_3 from melamine pyrolysis will help protect the textures of M-CA, which is thermally etched into 3D CN*l* with porous hierarchical structure due to the release of various gases. In addition, the samples obtained under the identical condition except for different solvent volume also exhibit similar 3D porous hierarchical structure (Fig. S6~8). The preferential decomposition of melamine can be verified by TGA-DSC analysis as shown in Fig. S3, both melamine and M-CA complexes without ethanol washing show weight loss at around 260 °C, while M-CA complexes washed with ethanol exhibits
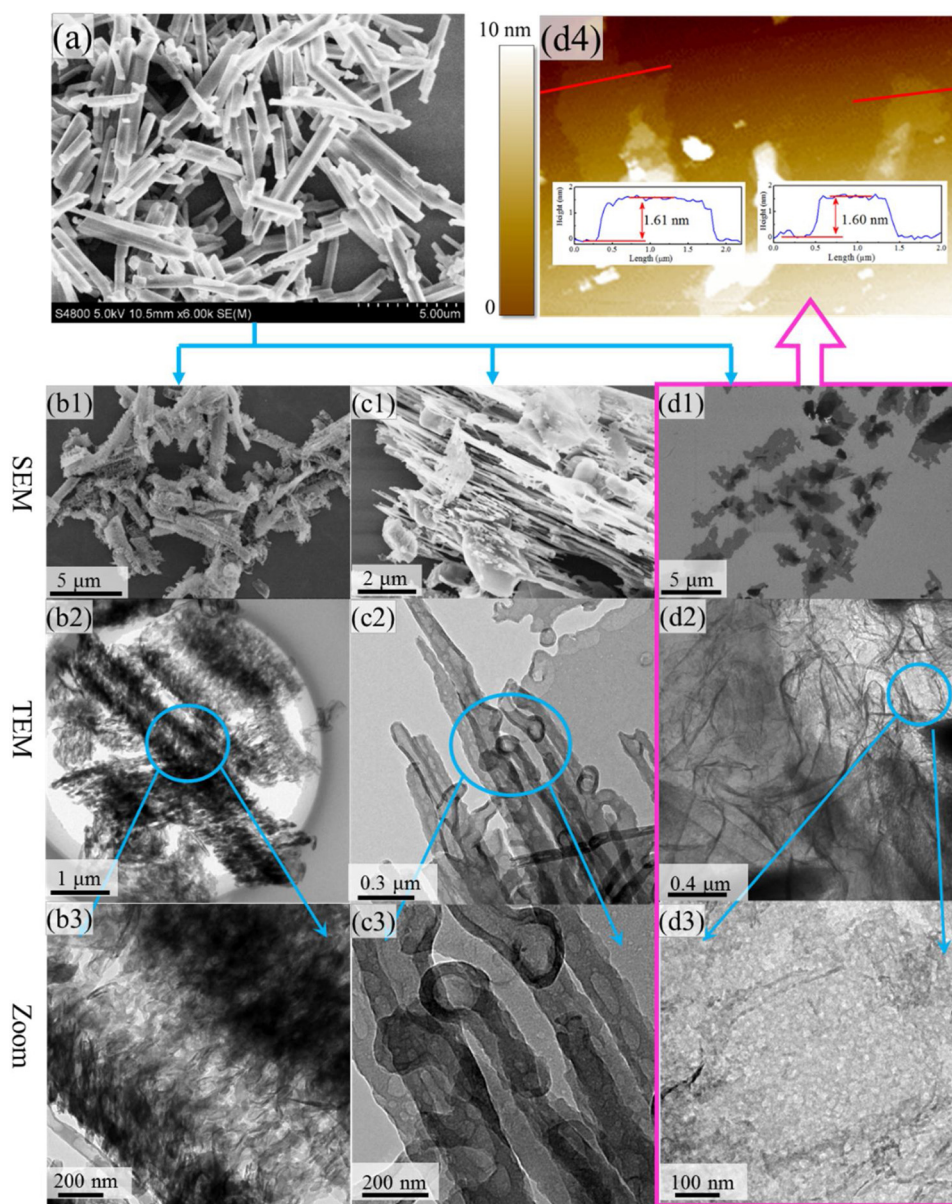
Fig. 2. Micromorphology and structure of different dimensions g-C$_3$N$_4$ prepared from hexagonal prism precursors. SEM and TEM of (a) M-CA complex, (b) CN*l*, (c) CN*t* (d) CN*s* and (d4) AFM of CN*s*. The M-CA complex presents a uniform hexagonal prism, which was obtained by used the melamine (M) and cyanuric acid (CA) in hot water (90 °C). Further, different treatment methods were used to obtain porous hierarchical self-supporting hollow 3D CN*l*, porous 2D ultrathin CN*s* and ordered porous 1D CN*t* array.

onset weight loss at higher temperature at about 320 °C, indicating that the free melamine on the M-CA complexes surface preferentially decomposes.

While the residual free melamine molecules adsorbed on M-CA complexes can be removed via ethanol washing. As the washed M-CA complexes are heated in the crucible covered and wrapped with tin foil, the M-CA complexes basically keep its original appearance but the size become small at about 400 °C during the process of thermal treatment, which is related to the formation of tri-s-triazine with various gases releasing including CO$_2$ and NH$_3$, and then condense into irregular blocks at temperature at 500 °C. Further condensation leads to the formation of 1D nanotubes ordered arrays(CN*t*) owing to thermal etching of the released gases. The M-CA complexes are also washed three times with 90 °C hot water and dried at 60 °C for two days. Then, the dried M-CA complexes are placed in a crucible wrapped with tin foil and calcined at 500 °C for 2 h under air atmosphere. Finally, similar 1D nanotube array of g-C$_3$N$_4$ can be obtained as shown in Fig. S13, which is

similar to that obtained from M-CA complex washed with ethanol. In addition, g-C$_3$N$_4$ from M-CA complex equimolecular ratio of melamine and cyanuric acid (1 : 1) in water also shows 1D nanotube array Fig. S14. On the contrary, higher molar ratio of melamine and cyanuric acid will lead to the mixture of different g-C$_3$N$_4$ morphologies(Fig. S10). These results verify the protective effect of moderate residual melamine on the textures of 3D g-C$_3$N$_4$ loofah-like architectures.

Unexpectedly, as the washed M-CA complexes are heated under N$_2$ atmosphere, the hexagonal prism M-CA complexes become irregular blocks at the temperature of 400°C due to pyrolysis, which may be attributed to the lack of protection of NH$_3$ on the textures of M-CA since the released gases are drawn away with N$_2$ flow. Further increasing temperature results in microvoids due to thermal etching, and is favor of N$_2$ diffusion. The thermal condensation between interlayers is suppressed owing to the inhibitory effect of N$_2$ molecules (Fig. S4). Then they thermal condense into product with cocoons-like morphology which is composed of thin layers(the lower panel of Fig. 3) with the
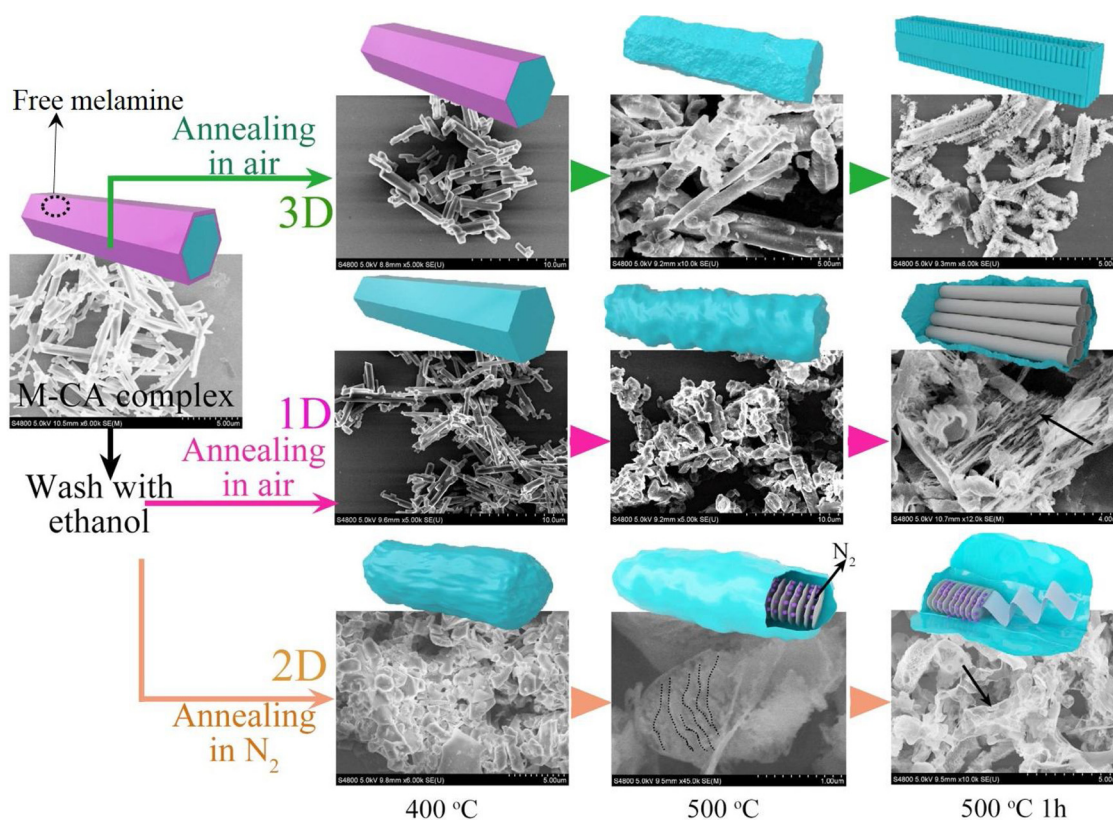
Fig. 3. The evolution process and conjectural mechanism of M-CA complex in the process of heating. The first, second, and third lines are the SEM images and speculative models of 3D CN*l*, 1D CN*t* and 2D CN*s* at different temperatures, respectively. The final 3D CN*l* and ordered 1D CN*t* array were obtained by annealing M-CA complex at 500 °C in air for 2 h. The final 2D CN*s* was obtained by annealing M-CA complex at 500 °C in N_2 for 3 h. All of the above heating rates are controlled at 5 °C min^{-1}.

temperature increase. As the heat treatment time increases, 2D CN*s* with a thickness of less than 2.0 nm are formed owing to further thermal condensation(Fig. 2 and S5). More importantly, the strategy results in high-quality, ultrathin CN nanosheet at yields of ~10 wt%, which is much higher than that of previous reports. This new strategy to prepare nanosheets is completely different from previous methods. In addition, the yields of CN*l* and CN*t* are up to about 16 wt% and 12 wt%, respectively(Table S2).

The crystal structure of as-synthesized g-C$_3$N$_4$ from melamine and supramolecular precursors were first characterized by XRD patterns and FT-IR spectroscopy. As shown Fig. 4a, b, the XRD patterns and FT-IR spectra of all samples are very similar, confirming that the general structure of g-C$_3$N$_4$ is preserved regardless of the post thermal treatment. The bulk CN synthesized from melamine at 500 °C, exhibits typical two diff ;raction peaks at around 13.0° (100) and 27.5° (002) (Fig. 4a), corresponding to the in-plane structural packing motif and the stacking of the conjugated aromatic systems, respectively. While the (002) peak of CN obtained from supramolecular precursor displays a slight shift to higher angles (Fig. 4a), indicating the reduction of the interlayer spacing and formation of a more condensed g-C$_3$N$_4$. The smaller spacing leads to the stronger interaction between the layers, which would enhance the charge transfer capability through the interface [59]. The FT-IR spectra of all samples (Fig. 4b) show broad peaks assigned to amine groups or hydroxy between 3000 and 3500 cm^{-1}, stretching modes of typical aromatic CN heterocycles from 1200–1600 cm^{-1}, and a typical breathing mode of the triazine units at 807 cm^{-1}, revealing their similar chemical structures. The C=O bonds appeared at 1720 cm^{-1} in the FT-IR spectra(Fig. 4b) indicate that oxygen atoms exist in the skeleton structure of CN*t* and CN*s*. In addition, the peak at 1242 cm^{-1} of bulk CN associated with stretching vibration of C−N bond shifts to 1248 cm^{-1} for CN*t* and CN*s*, which further

verify that part of C−N is transformed into C−O since the stretching vibration peak of C−N bond appears at higher wavenumber due to the higher electronegativity of O atoms [60]. The oxygen doping will cause a red shift in the absorption spectrum, which is beneficial to improve the catalytic performance.

The surface elemental compositions of CN*s* are further investigated by using XPS, which exhibit that the sample contains carbon, nitrogen and oxygen elements without other impurities. As shown in Fig. 4c, the C 1s peak position of CN*s* is located at 288.3 eV and 286.5 eV, indicating that the bonding structure is mainly sp2-bonded carbon N−C=N and slight C−NH in g-C$_3$N$_4$ [61]. In addition, the peak position at 284.8 eV can be attributed to the signal of C−C bonds of graphitic carbon impurities. The N 1s XPS spectrum of CN*s* (Fig. 4d) shows that the N 1s peak can be divided into three peaks located at 400.9 eV (N-H), 399.7 eV (N-(C)$_3$) and 398.6 eV (C−N=C). The O 1s high-resolution XPS spectrum could be deconvoluted into two different peaks, where the main peaks are attributed to the adsorbed water and the minor peaks are assigned to the C−O with binding energies at 532.5 and 530.8 eV, respectively (Fig. 4e) [62], further confirming the oxygen doping in CN*s*.

To elucidate the effects of geometric dimensionality and morphology on the properties of g-C$_3$N$_4$, the photocatalytic HER performance of all the samples was investigated under visible light irradiation (λ > 420 nm). Fig. 4f shows that all the polymeric g-C$_3$N$_4$ prepared from supramolecular precursors possess enhanced H$_2$ evolution activities in comparison with bulk CN. In particular, the porous ultrathin CN*s* show a dramatically high H$_2$ evolution activity (23.9 μmol h^{-1}), which is circa 17.3 times higher than that of bulk CN. Also, CN*t* exhibits a higher activity (8.87 μmol h^{-1}) than CN*l* (3.6 μmol h^{-1}) but still much higher than that of bulk CN. Moreover, the photocatalytic stability of CN*s* is investigated over 25 h with 5 successive cycles (Fig.
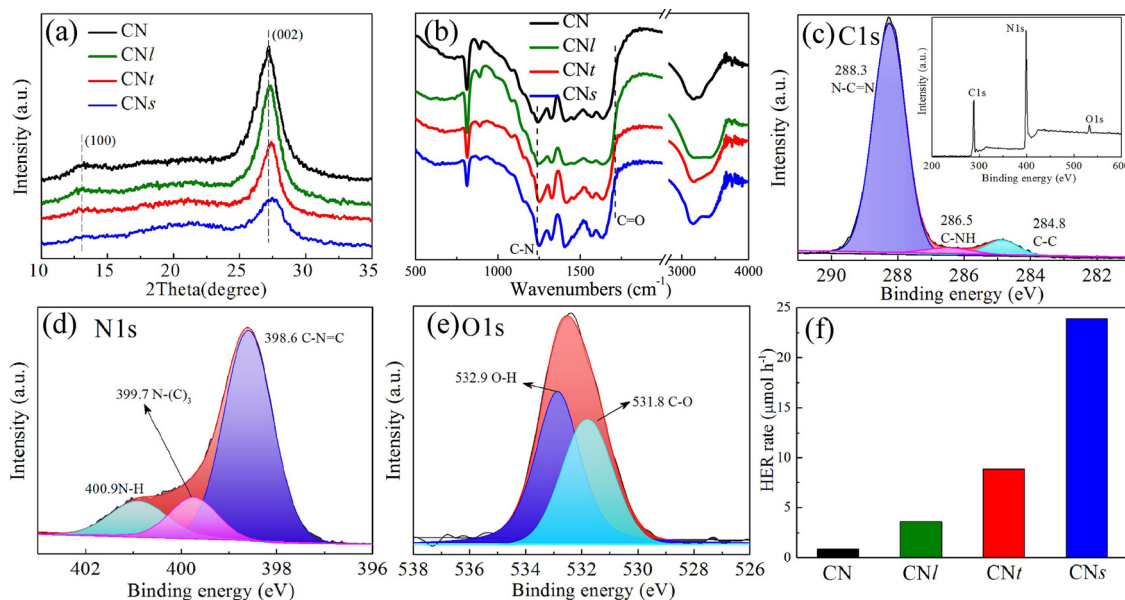
Fig. 4. (a) XRD patterns, (b) FT-IR spectra, (c˜e) XPS survey spectra: C1 s, N1 s, O1 s of the CN*s*, (f) Photocatalytic hydrogen evolution with 10 vol% methyl alcohol aqueous solution, 1 wt% Pt as a co-catalyst and 50 mg photocatalysts under visible light (λ > 420 nm) irradiation.

S22). There is no detectable decrease of the H_2 production, indicative of the good stability of CN*s*.

To further study the specific surface area and porours structure of synthetic simples, the nitrogen adsorption-desorption isotherms and Barret-Joyner-Halenda (BJH) pore size distribution curves are firstly tested. As shown in Fig. 5a, the nitrogen adsorption–desorption isotherms of CN*l*, CN*t* and CN*s* are all of representative type-IV curve with a H3-type hysteresis loops, which indicate the presence of abundant mesopores and a bit macropores in these three products. The pore size distribution (inset of Fig. 5a) of all the samples is from 10 nm to 100 nm, showing the characteristic of main hierarchical mesoporous and slight macroporous (sample stacking) structures. And the higher pore-size distribution curve of CN*t* indicates more porous structure than CN*l*, due to its more compact packing of 1D CN*t*. By contrast, a broad and obvious peak (30–100 nm) can be observed for CN*s*, which can be ascribed to the slit-shaped mesopores and abundant macropores formed

by the stacking of 2D ultrathin nanosheets structures. Therefore, the CN*s* possess a large pore volume of 0.83 $cm^3 g^{-1}$ (Table 1). The BET specific surface areas of CN*l*, CN*t* and CN*s* are calculated to be 51.5, 58.5, and 208.8 $m^2 g^{-1}$, respectively; which are much higher than bulk CN (8.0 $m^2 g^{-1}$). [63] The larger BET specific surface area can provide more active sites for adsorption and reaction; meanwhile hierarchical porous structure can facilitate the kinetics of reaction by facilitating the diffusion of reactants and products. Both of them are more beneficial to the photocatalytic HER.

The electronic band structures of all samples are investigated by a combined analysis of the M–S plots and UV–vis absorption spectra to explore the mechanism of improved photocatalytic HER. Apparently, the M–S plots of CN, CN*l*, CN*t*, and CN*s* under various frequencies disclose the typical n-type characteristic of organic semiconductors owing to the positive slope of the linear plots (Fig. S21). More importantly, the derived flat-band potentials for CN, CN*l*, CN*t*, and CN*s* are
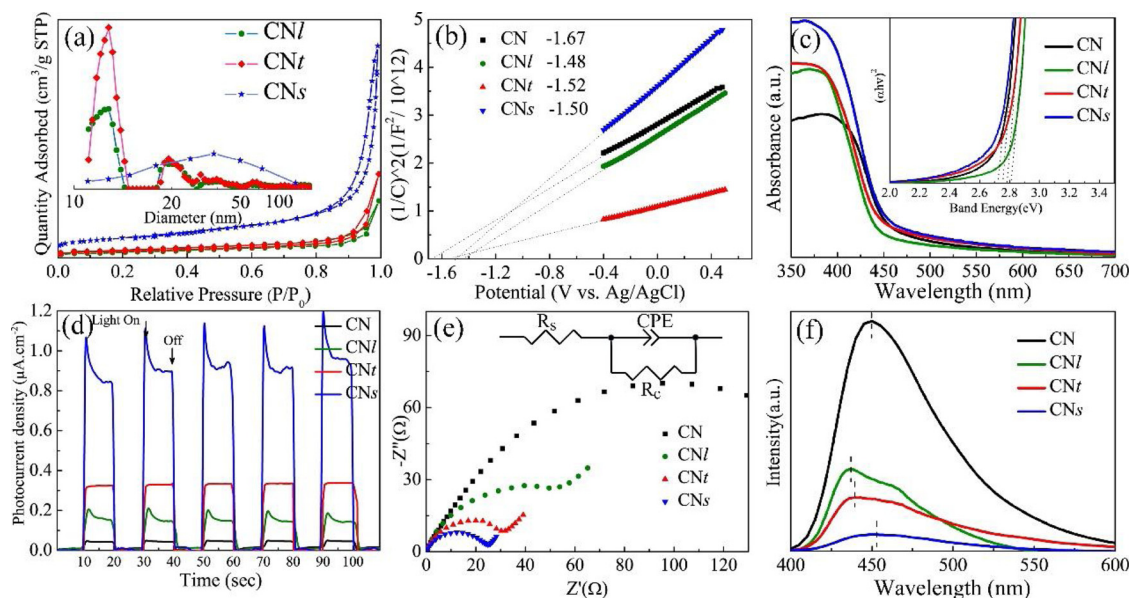
Fig. 5. (a) Nitrogen adsorption-desorption isotherm and pore size distribution of the samples, (b) Mott–Schottky plots, (c) UV–vis diffuse reflection spectra, (d) Photocurrent responses of samples under visible light irradiation; (e) EIS Nyquist plots and (f) PL spectra.

Table 1

BET specific surface area, total pore volume, charge transfer resistance (R_c), band gap (E_g), calculated E_{cb} and E_{vb}, and photocatalytic activity of the 50 mg samples for HER with simulated solar light and visible light ($\lambda > 420\,nm$) irradiation.

Sample	BET ($m^2 g^{-1}$)	Total pore volume ($cm^3 g^{-1}$)	R_c (Ω)	Band gap (eV)	E_{cb} (eV)	E_{vb} (eV)	HER(simulated solar light) [μmol h^{-1}]	HER (visible light) [μmol h^{-1}]
Bulk CN	8.0	–	199.8	2.76	−1.67	1.09	31.0	1.4
CNl	51.5	0.20	90.6	2.81	−1.48	1.33	92.0	3.6
CNt	58.5	0.72	41.6	2.78	−1.52	1.26	171.3	8.87
CNs	208.8	0.83	28.2	2.73	−1.50	1.23	258.7	23.9

about 1.67, 1.48, 1.52, and 1.50 V versus Ag/AgCl (Fig. 5b), suggesting that they are thermodynamically evident for photocatalytic reduction of water (H$^+$/H$_2$: −0.604 V vs. Ag/AgCl at pH 6.9). Furthermore, in comparison with bulk CN, the absorption edges of CNl and CNt are shifted to shorter wavelengths, the absorption edges of CNs are slightly shifted to longer wavelengths, as displayed in Fig. 5c. The band gap (E_g) is determined from $(\alpha h\nu)^2$ versus photon energy plots, as shown in the inset of Fig. 5c [64]. Based on Tauc plots, the band gaps for bulk CN, CNl, CNt and CNs are found to be 2.76, 2.81, 2.78 and 2.73 eV, respectively. These results reflect the competition effects of quantum size effect and oxygen doping on the optical properties.

To access the electric and photoelectric properties, transient photocurrent measurements for all samples are performed. Fig. 5d reveals that compared to bulk CN, those samples obtained from supramolecular precursors display a larger photocurrent under visible light irradiation. The photocurrent values are about 0.05, 0.20, 0.32, and 0.90 mA cm^{-2} for CN, CNl, CNt, and CNs, respectively, which is consistent with the trend seen in their HER activities. The highest photocurrent in CNs reflects the best visible-light response and highest efficient photoexcited charge separation. Moreover, the improved charge transport in g-C$_3$N$_4$ from supramolecular precursors can be very classically confirmed by the reduced hemicycle radius measured by using electrochemical impedance spectroscopy (EIS), as shown in Fig. 5e, which gives the order of hemicycle radius: CN > CNl > CNt > CNs. The charge transfer resistance calculated with an equivalent circuit (inset in Fig. 5e) are 199.8, 90.6, 41.6, and 28.2 Ω for CN, CNl, CNt, and CNs, respectively (Table 1). The small charge transfer resistance would beneficial to charge migration and separation to reduce the energy-wasteful recombination. This can be further verified by photoluminescence (PL) spectra, which is an effective strategy to characterize the separation and recombination efficiency of photogenerated charge carriers [65]. As displayed in Fig. 5f, the intrinsic PL emissions with the optical energy are close to the band gap energy of UV–vis absorption spectra. The CN exhibits a strong and broad emission peak centered at ≈ 450 nm at an excitation wavelength of 350 nm. On the contrary, the PL intensities of CNl, CNt and CNs are decreased greatly, indicating that the recombination rates of photoinduced electrons and holes are obviously suppressed.

Different from previous reports about supramolecular strategy, our study aff;ords a new approach for facile and effective regulation of the geometric dimensionality, morphology, and electronics simultaneously of g-C$_3$N$_4$. The superior photocatalytic HER of the synthesized ultrathin CNs can be attributed to the following aspects: (I) The porous CNs with enlarged surface area is of great benefit for fast mass transport and exposed surface active sites; (II) The ultrathin nanosheet (1.6 nm) significantly shortens the perpendicular migration distance of photogenerated charge from the bulk to the surface, and improve photogenerated charge transport ability along the in-plane direction; (III) The abundant holes on the nanosheets surface result in more active sites and exposed surface area; (IV) The dimensional and morphological transformation tune the electronic structure to enhance light harvesting and further improve the charge migration and separation, as verified by various tests.

4. Conclusions

In conclusion, we have, for the first time, presented a simple and promising strategy to regulate the geometric dimensionality, morphology, and electronics simultaneously of g-C$_3$N$_4$ using the M−CA complexes via the post thermal treatment. The new approach enables the controlled transformation of 3D precursors into 2D nanosheets and 1D nanotubes with large surface area. As a result, this method achieves synergistically dimensional, morphologic, and band gap, leading to the simultaneous improvement of the mass transport, active sites and conductivity as well as the optical absorption for the HER. Thanks to the above benefits, the resulting 2D ultrathin CNs from precursors display much superior photocatalytic HER to the bulk CN under both simulated sunlight and visible light, which bring additional opportunities for the manipulation of aromatic p-conjugated systems for advanced applications. The proposed strategy of dimensionality and morphology modulation is expected to broaden our horizons in designing novel highly-active photocatalysts for a variety of energy-related applications.

Competing interest

The authors declare no competing financial interest.

Acknowledgements

Appendix A. Supplementary data

Supplementary material related to this article can be found, in the online version, at doi:https://doi.org/10.1016/j.apcatb.2019.05.015.

References

[1] Z.Y. Lin, Y. Liu, U. Halim, M.N. Ding, Y. Liu, Y.L. Wang, C.C. Jia, P. Chen, X.D. Duan, C. Wang, F. Song, M.F. Li, C.Z. Wan, Y. Huang, X.F. Duan, Nature 562 (2018) 254–258.
[2] D. Wang, W.W. Zhou, R. Zhang, J.J. Zeng, Y. Du, S. Qi, C.X. Cong, C.Y. Ding, X.X. Huang, G.W. Wen, T. Yu, Adv. Mater. 30 (2018) 1803569.
[3] J.E. Kim, J.H. Oh, M. Kotal, N. Koratkar, I.K. Oh, Nano Today 14 (2017) 100–123.
[4] K.S. Kumar, N. Choudhary, Y. Jung, J. Thomas, ACS Energy Lett. 3 (2018) 482–495.
[5] D. Voiry, H. Yamaguchi, J.W. Li, R. Silva, D.C.B. Alves, T. Fujita, M.W. Chen, T. Asefa, V.B. Shenoy, G. Eda, M. Chhowalla, Nat. Mater. 12 (2013) 850–855.
[6] J. Tian, R. Ning, Q. Liu, A.M. Asiri, A.O. Al-Youbi, X. Sun, ACS Appl. Mater. Interfaces 6 (2014) 1011–1017.
[7] J.N. Qin, S.B. Wang, H. Ren, Y.D. Hou, X.C. Wang, Appl. Catal. B 179 (2015) 1–8.
[8] Y.J. Cui, Z.X. Ding, X.Z. Fu, X.C. Wang, Angew. Chem. Int. Ed. 51 (2012) 11814–11818.
[9] Y. Chen, C.L. Tan, H. Zhang, L.Z. Wang, Chem. Soc. Rev. 44 (2015) 2681–2701.
[10] C.L. Tan, P. Yu, Y.L. Hu, J.Z. Chen, Y. Huang, Y.Q. Cai, Z.M. Luo, B. Li, Q.P. Lu, L.H. Wang, Z. Liu, H. Zhang, J. Am. Chem. Soc. 137 (2015) 10430–10436.
[11] M.R. Alenezi, S.J. Henley, N.G. Emerson, S.R.P. Silva, Nanoscale 6 (2014) 235–247.
[12] S.B. Yang, Y.J. Gong, J.S. Zhang, L. Zhan, L.L. Ma, Z.Y. Fang, R. Vajtai, X.C. Wang, P.M. Ajayan, Adv. Mater. 25 (2013) 2452–2456.
[13] Z. Yang, Y.J. Zhang, Z. Schnepp, J. Mater. Chem. A Mater. Energy Sustain. 3 (2015) 14081–14092.
[14] Z. Sun, T. Liao, Y. Dou, S.M. Hwang, M.-S. Park, L. Jiang, J.H. Kim, S.X. Dou, Nat. Commun. 5 (2014) 3813.

[15] K. Liang, K. Marcus, S.F. Zhang, L. Zhou, Y.L. Li, S.T. De Oliveira, N. Orlovskaya, Y.H. Sohn, Y. Yang, Adv. Energy Mater. 7 (2017) 1701309.
[16] T.W. Kim, S.J. Hwang, S.H. Jhung, J.S. Chang, H. Park, W. Choi, J.H. Choy, Adv. Mater. 20 (2008) 539–542.
[17] S. Pedireddy, H.K. Lee, W.W. Tjiu, I.Y. Phang, H.R. Tan, S.Q. Chua, C. Troadec, X.Y. Ling, Nat. Commun. 5 (2014) 4947.
[18] J.Q. Tian, Q. Liu, C.J. Ge, Z.C. Xing, A.M. Asiri, A.O. Al-Youbi, X.P. Sun, Nanoscale 5 (2013) 8921–8924.
[19] J.Q. Tian, Q. Liu, A.M. Asiri, K.A. Alamry, X.P. Sun, ChemSusChem 7 (2014) 2125–2130.
[20] W. Niu, Y. Yang, ACS Energy Lett. 3 (2018) 2796–2815.
[21] J. Ran, T.Y. Ma, G. Gao, X.-W. Du, S.Z. Qiao, Energy Environ. Sci. 8 (2015) 3708–3717.
[22] T.Y. Ma, S. Dai, M. Jaroniec, S.Z. Qiao, Angew. Chem. Int. Ed. 53 (2014) 7281–7285.
[23] X.C. Wang, K. Maeda, A. Thomas, K. Takanabe, G. Xin, J.M. Carlsson, K. Domen, M. Antonietti, Nat. Mater. 8 (2009) 76–80.
[24] Y. Zheng, J. Liu, J. Liang, M. Jaroniec, S.Z. Qiao, Energy Environ. Sci. 5 (2012) 6717–6731.
[25] N. Cheng, J. Tian, Q. Liu, C. Ge, A.H. Qusti, A.M. Asiri, A.O. Al-Youbi, X. Sun, ACS Appl. Mater. Interfaces 5 (2013) 6815–6819.
[26] Y.X. Fang, X.C. Wang, Chem. Commun. 54 (2018) 5674–5687.
[27] Z. Wang, X. Hu, G. Zou, Z. Huang, Z. Tang, Q. Liu, G. Hu, D. Geng, Sustain. Energy Fuels 3 (2019) 611–655.
[28] S. Zhao, Y. Zhang, Y. Zhou, Y. Wang, K. Qiu, C. Zhang, J. Fang, X. Sheng, Carbon 126 (2018) 247–256.
[29] D. Zheng, C. Pang, Y. Liu, X. Wang, Chem. Commun. 51 (2015) 9706–9709.
[30] Y. Wang, Y. Li, W. Ju, J. Wang, H. Yao, L. Zhang, J. Wang, Z. Li, Carbon 102 (2016) 477–486.
[31] X.-H. Li, X. Wang, M. Antonietti, Chem. Sci. 3 (2012) 2170–2174.
[32] X.-H. Li, J. Zhang, X. Chen, A. Fischer, A. Thomas, M. Antonietti, X. Wang, Chem. Mater. 23 (2011) 4344–4348.
[33] Y. Zheng, L.H. Lin, X.J. Ye, F.S. Guo, X.C. Wang, Angew. Chem. Int. Ed. 53 (2014) 11926–11930.
[34] L. Ma, H. Fan, J. Wang, Y. Zhao, H. Tian, G. Dong, Appl. Catal. B 190 (2016) 93–102.
[35] Q. Han, B. Wang, J. Gao, Z.H. Cheng, Y. Zhao, Z.P. Zhang, L.T. Qu, ACS Nano 10 (2016) 2745–2751.
[36] Q. Qiao, K. Yang, L.L. Ma, W.Q. Huang, B.X. Zhou, A.L. Pan, W.Y. Hu, X.X. Fan, G.F. Huang, J. Phys. D Appl. Phys. 51 (2018) 275302.
[37] S. Guo, Z. Deng, M. Li, B. Jiang, C. Tian, Q. Pan, H. Fu, Angew. Chem. Int. Ed. 55 (2016) 1830–1834.
[38] F. He, G. Chen, J.W. Miao, Z.X. Wang, D.M. Su, S. Liu, W.Z. Cai, L.P. Zhang, S. Hao, B. Liu, ACS Energy Lett. 1 (2016) 969–975.
[39] S.E. Guo, Y.Q. Tang, Y. Xie, C.G. Tian, Q.M. Feng, W. Zhou, B.J. Jiang, Appl. Catal. B 218 (2017) 664–671.
[40] P.J. Yang, H.H. Ou, Y.X. Fang, X.C. Wang, Angew. Chem. Int. Ed. 56 (2017) 3992–3996.
[41] J.Q. Tian, Q. Liu, A.M. Asiri, A.H. Qusti, A.O. Al-Youbi, X.P. Sun, Nanoscale 5 (2013) 11604–11609.
[42] X. Zhang, X. Xie, H. Wang, J. Zhang, B. Pan, Y. Xie, J. Am. Chem. Soc. 135 (2013) 18–21.
[43] X.J. She, L. Liu, H.Y. Ji, Z. Mo, Y.P. Li, L.Y. Huang, D.L. Du, H. Xu, H.M. Li, Appl. Catal. B 187 (2016) 144–153.
[44] S. Samanta, R. Srivastava, Sustain. Energy Fuels 1 (2017) 1390–1404.
[45] P. Xia, B. Zhu, J. Yu, S. Cao, M. Jaroniec, J. Mater. Chem. A Mater. Energy Sustain. 5 (2017) 3230–3238.
[46] J. Zhang, Y. Chen, X. Wang, Energy Environ. Sci. 8 (2015) 3092–3108.
[47] J. Xu, D. Zhang, R. Shi, Y. Zhu, J. Mater. Chem. A Mater. Energy Sustain. 1 (2013) 14766–14772.
[48] P. Niu, L. Zhang, G. Liu, H.-M. Cheng, Adv. Funct. Mater. 22 (2012) 4763–4770.
[49] M. Shalom, M. Guttentag, C. Fettkenhauer, S. Inal, D. Neher, A. Llobet, M. Antonietti, Chem. Mater. 26 (2014) 5812–5818.
[50] S. Wan, M. Ou, Q. Zhong, S. Zhang, W. Cai, Adv. Opt. Mater. 5 (2017) 1700536.
[51] Y.Y. Li, S.F. Ma, B.X. Zhou, W.Q. Huang, X.X. Fan, X.F. Li, K. Li, G.F. Huang, J. Phys. D Appl. Phys. 52 (2019) 105502.
[52] Y.Q. Tang, M. Yuan, B.J. Jiang, Y.T. Xiao, Y. Fu, S. Chen, Z.P. Deng, Q.J. Pan, C.G. Tian, H.G. Fu, J. Mater. Chem. A Mater. Energy Sustain. 5 (2017) 21979–21985.
[53] Y. Guo, J. Li, Y. Yuan, L. Li, M. Zhang, C. Zhou, Z. Lin, Angew. Chem. Int. Ed. 55 (2016) 14693–14697.
[54] C. Zhou, C. Lai, D. Huang, G. Zeng, C. Zhang, M. Cheng, L. Hu, J. Wan, W. Xiong, M. Wen, X. Wen, L. Qin, Appl. Catal. B 220 (2018) 202–210.
[55] Y.-S. Jun, E.Z. Lee, X. Wang, W.H. Hong, G.D. Stucky, A. Thomas, Adv. Funct. Mater. 23 (2013) 3661–3667.
[56] D. Wang, S. Li, Q. Feng, J. Mater. Sci. - Mater. Electron. 29 (2018) 9380–9386.
[57] M. Shalom, S. Inal, C. Fettkenhauer, D. Neher, M. Antonietti, J. Am. Chem. Soc. 135 (2013) 7118–7121.
[58] J.-W. Zhang, S. Gong, N. Mahmood, L. Pan, X. Zhang, J.-J. Zou, Appl. Catal. B 221 (2018) 9–16.
[59] L.H. Lin, W. Ren, C. Wang, A.M. Asiri, J. Zhang, X.C. Wang, Appl. Catal. B 231 (2018) 234–241.
[60] P. Qiu, C. Xu, H. Chen, F. Jiang, X. Wang, R. Lu, X. Zhang, Applied Catalysis B-Environmental 206 (2017) 319–327.
[61] X.P. Song, Q. Yang, X.H. Jiang, M.Y. Yin, L.M. Zhou, Appl. Catal. B 217 (2017) 322–330.
[62] B. Luo, R. Song, J.F. Geng, D.W. Jing, Y.Z. Zhang, Appl. Catal. B 238 (2018) 294–301.
[63] S.C. Yan, Z.S. Li, Z.G. Zou, Langmuir 25 (2009) 10397–10401.
[64] J. Liu, Y. Liu, N. Liu, Y. Han, X. Zhang, H. Huang, Y. Lifshitz, S.-T. Lee, J. Zhong, Z. Kang, Science 347 (2015) 970–974.
[65] Y. Kang, Y. Yang, L.-C. Yin, X. Kang, L. Wang, G. Liu, H.-M. Cheng, Adv. Mater. 28 (2016) 6471–6477.